

Enhanced loss of magnetic-mirror-trapped fast electrons by a shear Alfvén wave^{a)}

Y. Wang, W. Gekelman, P. Pribyl, and K. Papadopoulos

Citation: *Physics of Plasmas* (1994-present) **21**, 055705 (2014); doi: 10.1063/1.4874332

View online: <http://dx.doi.org/10.1063/1.4874332>

View Table of Contents: <http://scitation.aip.org/content/aip/journal/pop/21/5?ver=pdfcov>

Published by the [AIP Publishing](#)

Articles you may be interested in

[On nonlinear physics of shear Alfvén waves^{a\)}](#)

Phys. Plasmas **20**, 055402 (2013); 10.1063/1.4804628

[Development of polarization-controlled multi-pass Thomson scattering system in the GAMMA 10 tandem mirror^{a\)}](#)

Rev. Sci. Instrum. **83**, 10E333 (2012); 10.1063/1.4734490

[The many faces of shear Alfvén waves^{a\)}](#)


Phys. Plasmas **18**, 055501 (2011); 10.1063/1.3592210


[Doppler-shifted cyclotron resonance of fast ions with circularly polarized shear Alfvén waves^{a\)}](#)

Phys. Plasmas **16**, 055706 (2009); 10.1063/1.3103813


[Prospects of ion beam extraction and transport simulations \(invited\)^{a\)}](#)

Rev. Sci. Instrum. **79**, 02B716 (2008); 10.1063/1.2823968

A collection of five pieces of Pfeiffer Vacuum equipment, including a red turbopump, a silver turbopump, a silver backing pump, a red leak detector, and a silver measurement and analysis chamber.

 Vacuum Solutions from a Single Source

- Turbopumps
- Backing pumps
- Leak detectors
- Measurement and analysis equipment
- Chambers and components

PFEIFFER  **VACUUM**

Enhanced loss of magnetic-mirror-trapped fast electrons by a shear Alfvén wave^{a)}

Y. Wang,^{1,b)} W. Gekelman,¹ P. Pribyl,¹ and K. Papadopoulos²

¹Department of Physics and Astronomy, University of California, Los Angeles, California 90095, USA

²Department of Physics and Astronomy, University of Maryland, College Park, Maryland 20742, USA

(Received 12 December 2013; accepted 25 February 2014; published online 1 May 2014)

Laboratory observations of enhanced loss of magnetic mirror trapped fast electrons irradiated by a shear Alfvén Wave (SAW) are reported. The experiment is performed in the quiescent after-glow plasma in the Large Plasma Device [Gekelman *et al.*, Rev. Sci. Instrum. **62**(12), 2875–2883 (1991)]. A trapped energetic electron population (>100 keV) is generated in a magnetic mirror section (mirror ratio ≈ 2 , length = 3.5 m) by an X-mode high power microwave pulse, and forms a hot electron ring due to the grad-B and curvature drift. SAWs of arbitrary polarization are launched externally by a Rotating Magnetic Field source ($\delta B/B_0 \approx 0.1\%$, $\lambda_{\parallel} \approx 9$ m). Irradiated by a right-handed circularly polarized SAW, the loss of electrons, in both the radial and the axial direction of the mirror field, is significantly enhanced and is modulated at $f_{\text{Alfvén}}$. The periodical loss continues even after the termination of the SAW. Experimental observations suggest that a spatial distortion of the ring is formed in the SAW field and creates a collective mode of the hot electron population that degrades its confinement and leads to electron loss from the magnetic mirror. The results could have implications on techniques of radiation belt remediation. © 2014 AIP Publishing LLC.

[<http://dx.doi.org/10.1063/1.4874332>]

I. INTRODUCTION

Highly energetic electrons in the Earth's radiation belts are frequently referred to as “killer electrons” for their ability to cause fatal radiation damage to satellites. The killer electron flux naturally exists as observed by extensive satellite measurements since the discovery of the radiation belts, and can be dramatically enhanced by human activity such as High Altitude Nuclear Explosions (HANEs). The need for protection of the communication infrastructure is receiving increasing attention in recent years with the fast growing application of satellite technology, represented by \$177.3 billion revenue of the global satellite industry in 2011, and an average annual growth rate of 10.7% for the past decade.² Passive actions to cope with the everyday hostile environment of space have already been taken, such as the expensive practice of radiation hardening often with redundancies in the electronics to prolong satellite lifetime. There is a great deal of current interest in developing artificial techniques to mitigate extraordinary energetic charged particle flux events.³ The topic has come to be known as “radiation belt remediation.” In this paper, we present a laboratory experiment in which a population of energetic electrons is trapped in a magnetic mirror field and subsequently irradiated by a shear Alfvén wave. It is observed that the low frequency ($f < f_{\text{ci}}$, f_{ci} is the ion cyclotron frequency) Alfvén wave dramatically affects the confinement, and the trapped electrons are scattered out of the magnetic mirror in both the radial and axial direction.

Aside from remediation, the experiment presented here is of general interest in space science. For example, one unanswered, fundamental question is which mechanism is primarily accounted for the natural loss of electrons in the radiation belt.⁴ Of special interest is the dramatic drop of the relativistic electron flux during geomagnetic storms when it can be decreased by several orders of magnitude within hours.^{5,6} Possible explanations include pitch-angle scattering through wave-particle interactions,^{7,8} magnetopause shadowing,^{9,10} rapid outward radial transport,^{11,12} to name a few. To answer such a question, detailed understanding of each of these processes is required. These processes are usually tangled in the space environment because they can occur simultaneously. It is difficult to evaluate the effectiveness of any single process, or even identify causality in this uncontrolled environment. Controlled laboratory experiments can separate these processes, and provide opportunities to study them in great detail, one-by-one. This experiment was designed to study the response of mirror-trapped electrons to a low frequency electromagnetic (EM) wave.¹³ This fundamental process is involved in phenomena such as the depletion of radiation belt electron flux,^{14–16} acceleration of energetic electrons in the radiation belts,^{17,18} and the modulation of VLF emissions¹⁹ to name a few.

This paper is organized as follows. Section II introduces the experimental setup, including the method adapted to generate a magnetic-mirror-trapped fast electron population and to launch arbitrarily polarized shear Alfvén waves. In Sec. III, major experimental observations are reported. A discussion of the experimental results and conjectures as to what the de-trapping mechanism is are presented in Sec. IV.

^{a)}Paper JI2 4, Bull. Am. Phys. Soc. **58**, 144 (2013).

^{b)}Invited speaker.

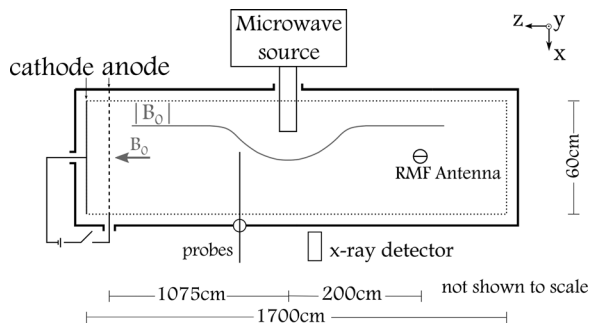


FIG. 1. Schematic of experimental setup (not to scale).

II. EXPERIMENTAL SETUP

A. The large plasma device

The experiment is performed at the Large Plasma Device (LaPD) at the University of California, Los Angeles.¹ The experimental setup is summarized in Fig. 1. The vacuum vessel of the device is a 22 m long, 1 m diameter cylindrical chamber encircled by co-axial solenoidal coils which provide a confining static magnetic field up to 3.5 kG. The electro-magnets are divided into 10 sets along the z-direction (magnetic axis) and driven by independently programmable power supplies to provide variable magnetic field configurations. In this experiment, a symmetric magnetic mirror field is established, with $B_{\min} = 438$ Gauss and $B_{\max} = 800$ G. The length of the mirror trap is 3.5 m measured between the two points where $B = 0.95 B_{\max}$. The background magnetic field profile on the machine axis, calculated from the current fed to the solenoids, is plotted in Fig. 2, where the magnetic mirror is centered near $z = 0$.

The LaPD plasma (diameter = 0.6 m, length = 17 m) is produced by a pulsed dc discharge (typically $V_d = 60$ V, $I_d = 3$ kA, 10 ms duration, 1 Hz repetition rate) between a heated cathode and a mesh anode located at one end of the device with a separation of 0.5 m. The anode is 10.75 m away from the center of the magnetic mirror. This experiment is conducted in the quiescent plasma after the dc discharge is switched off (plasma afterglow, see Fig. 3). The typical helium plasma used in this experiment has a density of $5 \times 10^{11} \text{ cm}^{-3}$ and an electron temperature of 0.5 eV, as measured by a swept Langmuir probe and a 60 GHz microwave interferometer. The discharge is highly reproducible, and is repeated every second for weeks, allowing data collection over a set of spatial locations by moving only one probe with a computer controlled data acquisition system.

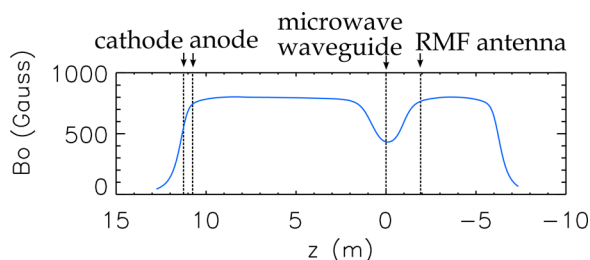


FIG. 2. The background magnetic field profile and locations of the LaPD cathode and mesh anode, ECRH input, and the SAW antenna.

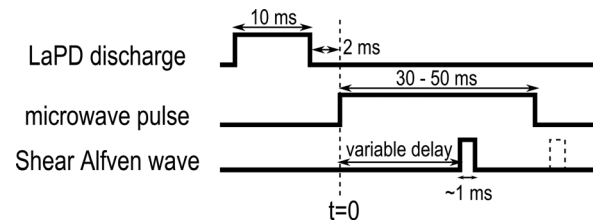


FIG. 3. Experimental timing scheme. The hot electron ring is generated by ECRH in the quiescent LaPD after-glow plasma after the dc discharge power is switched off.

B. Generation of a magnetic mirror-trapped hot electron ring

The background afterglow plasma is heated and a population of trapped fast electrons is generated by microwaves via Electron Cyclotron Resonance Heating (ECRH). At the center of the mirror, high power (1–15 kW) microwaves are introduced radially through a 10 cm diameter cylindrical waveguide. Different magnetic mirror field profiles were tested, and the ECRH was found to be most efficient at $f_{\text{microwaves}} = 2f_{ce}$ at the field minimum. In this experiment, the origin of the z-axis is defined by the axial location of the waveguide, and the origins of x and y axis are on the machine axis. The waveguide is inserted into the machine through a vacuum interlock along the negative x-axis; the end of the waveguide is located at $x = -15$ cm (Fig. 1). The microwaves are generated by a fixed frequency ($f_{\text{microwave}} = 2.45$ GHz) magnetron. The source is operated in a pulsed mode (1 Hz) at a peak power of 15 kW, with each pulse starting 2 ms after the LaPD discharge is turned off and lasting for 30–50 ms. The starting time of the microwave pulse is defined as $t = 0$. Fig. 3 summarizes the experimental timing scheme. The microwaves pass through a water-cooled ceramic vacuum window designed to minimize reflection, and propagate in the $TE_{1,1}$ mode with $\mathbf{E}_{\text{microwaves}} \parallel \mathbf{y}$ in the waveguide where the plasma density is negligible. The microwaves become extraordinary waves (X-mode) as they enter the plasma radially. The cold plasma dispersion approximation predicts that the X-mode wave is evanescent when the plasma density is above a critical density of $1.1 \times 10^{11} \text{ cm}^{-3}$ at the fixed background magnetic field of 438 G. In this case, the microwave field exponentially decays as it propagates into the plasma. The decay length decreases with increasing plasma density. At peak power, the electric field of the microwaves in the waveguide is 3×10^2 V/cm. In the afterglow plasma with a typical density of $n_e = 5 \times 10^{11} \text{ cm}^{-3}$, the decay length is calculated to be 5.3 cm. It has been observed that the heating is less effective during the LaPD discharge when plasma density is higher.

The ECRH heated plasma consists of a thermalized warm plasma component as well as a population of run-away hot electrons. For the warm plasma, the electron distribution can be well approximated by a Maxwellian, as seen in a Langmuir probe current-voltage characteristic curve. The warm plasma temperature is measured to be $T_e \leq 50$ eV, and plasma density is $n_e = (3 \pm 1) \times 10^{11} \text{ cm}^{-3}$.

The presence of the hot electron population is evidenced by detection of hard x-rays. The x-rays are generated when

the hot electrons strike metallic surfaces. Due to the imperfect confinement of the magnetic mirror, hot electrons are slowly lost and x-rays continuously generated. The x-rays are detected by a NaI(Tl) scintillator detector located outside the vacuum chamber, with a solid angle span of 0.004 sr (± 0.002 sr depending on its location) measured from the center of the magnetic mirror. The chamber wall is made of 3/8 in. thick stainless steel, which cuts off x-ray transmission below ~ 100 keV. The x-ray energies are determined to be in the range from 100 keV to 3 MeV using pulse height analysis of the scintillator detector response.

The magnetic mirror trapped hot electrons drift in the azimuthal direction due to the grad-B drift, which results in the formation of a hot electron ring within the mirror trap.²⁰ The electron confinement time (before a loss due to cumulative collisions with Helium atoms or ions) is much longer than the period of their grad-B and curvature drift motion ($\tau_{trapping}/\tau_{drift} > 5 \times 10^3$).

The radial thickness of the ring is measured using a “luminator probe.” The probe consists of a $5 \times 5 \times 1$ mm³ tungsten tip at the end of a 10 mm diameter ceramic shaft. Due to the high atomic number of tungsten, copious x-rays are generated when the hot electrons strike the tungsten tip. The thin ceramic shaft does not have the same effect. Fig. 4 is the measured x-ray flux as a function of the probe tip position when the probe is inserted from the positive x-axis. Far away from the ring (probe tip $x > 15$ cm), the probe has no effect on the x-ray production. A background x-ray flux is measured which is generated by hot electrons slowly lost from the mirror. The hot electron ring cannot form when the probe completely cuts through the ring region (probe tip $x < 5$ cm), therefore no x-rays are measured in these cases. The thickness of the ring is measured to be 10 cm.

By inserting the probe at different z locations, the axial extension of the ring is measured to be $\Delta z = 211$ cm, which is directly related to the electron anisotropy. The minimum pitch angle θ of a trapped electron is related to the furthest distance the electron travels in the axial direction z_{max} by

$$\tan \theta = 1 / \sqrt{\frac{B(z_{max})}{B_{min}} - 1},$$

where B_{min} is the minimum magnetic field in the mirror. The calculated lower limit of the pitch-angle distribution of all hot electrons is 56° . The loss cone angle for this magnetic mirror is 47° . The wide margin of the pitch-angle distribution to the loss cone indicates that the anisotropy of the

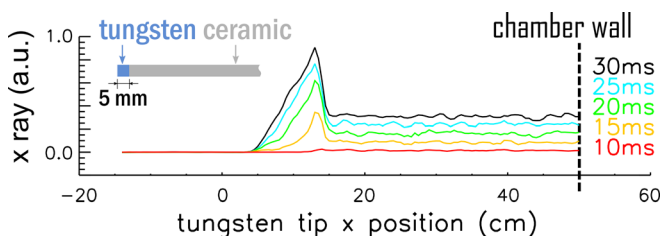


FIG. 4. X-ray flux as a function of luminator probe tungsten tip position, at different times during the ECRH denoted by the colored lines. The probe is inserted radially along the positive x axis.

electron velocity is less likely to be shaped by the magnetic confinement, but is dominated by the ECRH which primarily increases the electron’s perpendicular energy.

C. Launching shear Alfvén waves

Shear Alfvén waves (SAWs) are also known as Slow Alfvén waves or Torsional Alfvén waves. They propagate nearly parallel to \mathbf{B}_0 at a frequency below ω_{ci} (ion gyro-frequency). The propagation of SAW can be most concisely described in one of the two limits of $v_A/v_{Te} \gg 1$ (inertial) and $v_A/v_{Te} \ll 1$ (kinetic); here, $v_A = B/(4\pi n m_i)^{1/2}$ is the Alfvén speed and $v_{Te} = (kT_e/m_e)^{1/2}$ is the electron thermal speed.²¹ In this experiment, the wave is launched in the after-glow plasma with $v_A/v_{Te} \approx 4$, and is in the inertial SAW regime, which satisfies the dispersion relation²²

$$k_{\parallel}^2 = \omega^2 (1 + k_{\perp}^2 \delta^2) / [v_A^2 (1 - \omega^2 / \omega_{ci}^2)],$$

where k_{\parallel} and k_{\perp} are the parallel and perpendicular wave number, ω is the wave frequency, and $\delta = c/\omega_{pe}$ is the electron skin depth.

In this experiment, the shear Alfvén waves are launched externally using a Rotating Magnetic Field (RMF) antenna^{23,24} located at $z = -1.91$ m downstream from the center of the mirror section (Figs. 1 and 2). The antenna is composed of 2 orthogonal coils (normal to x and y direction) with diameters of 8 cm and 9 cm. Each of the two coils is driven independently from the other, giving the antenna the capability to launch waves with arbitrary polarization. The dispersion relation of SAW has been verified by experiment²³ and computer simulation²⁴ for the wave radiated by this RMF antenna in a uniform plasma.

In this experiment, the SAW propagation deviates from that in a uniform plasma by the existence of a varying B_0 profile in the mirror region (Fig. 2), where the SAW is launched at a frequency of $\bar{\omega} = 0.38$, and propagates to the center of the mirror field where $\bar{\omega} = 0.69$ (the scaled frequency $\bar{\omega} \equiv \omega/\omega_{ci}$). The magnetic field of the Alfvén wave is measured with 3-axis magnetic induction probes on two transverse planes at $z = 0$ and $z = 191.7$ cm, and shown in Fig. 5. The measured wave field inside the mirror exhibits a very similar pattern as that in the straight field section, with the exception of a perpendicular spread of the wave pattern due to the diverging magnetic field lines. The inertial SAW propagates nearly parallel to the ambient magnetic field. The angle that the wave group velocity deviates from the direction of background field, known as the cone angle,^{22,25} is calculated to be less than 0.15° thus is negligible in this experiment. The shear Alfvén wave measured at the center of the magnetic mirror has typical amplitude of 0.5 G ($B_{wave}/B_0 \approx 0.1\%$) almost perpendicular to B_0 . The estimated E_{wave} amplitude to the first order is 0.5 V/cm,²⁶ with $E_{\parallel}/E_{\perp} < 0.02$.

III. EXPERIMENTAL RESULTS

A. Overview

Due to the imperfect confinement, even in absence of the shear Alfvén wave, some trapped hot electrons are slowly

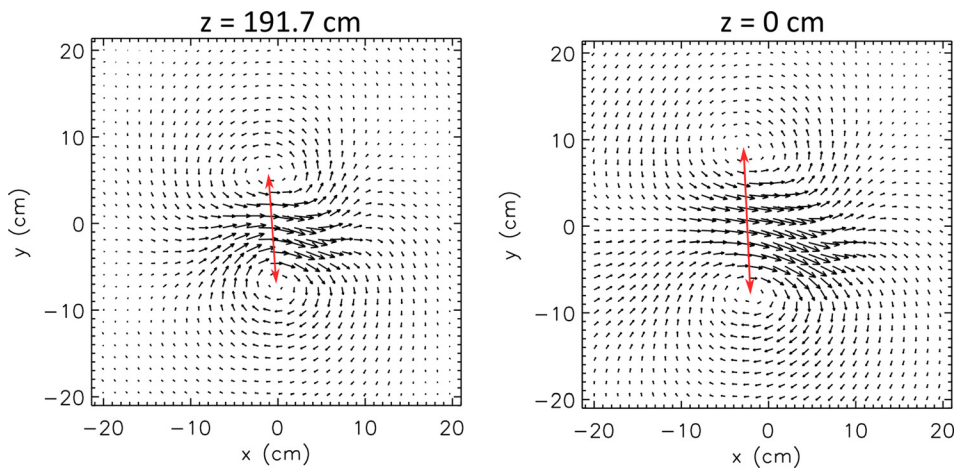


FIG. 5. SAW magnetic field vectors measured by B-dot probes inside/outside the magnetic mirror. The two planes are displayed for two different time instants, chosen with same wave phase for the ease of comparison. The wave exhibits a very similar pattern in the two regions with the exception of a perpendicular spread of the wave pattern. The distances between the two current channels in the two planes (marked by red arrows) are 13 cm and 17.5 cm, respectively. The RMF antenna is located at $z = -2$ m.

lost from the magnetic mirror and strike metallic objects in the vacuum chamber, producing a steady x-ray flux measurable outside the vacuum chamber. This is referred to as “the background x-ray production” and is shown in trace A in Fig. 6. It is thought that the background x-rays are related to the presence of the microwaves, as evidenced by the fact that their signal drops rapidly with the termination of the ECRH at $t = 30$ ms (it takes about 0.5 ms to completely turn off the ECRH).

In this series of experiments, it takes about 20 ms for a measurable background x-ray flux to be generated. We attribute this to the time it takes to accelerate a substantial electron population to energies that produce x-rays measurable outside the vacuum vessel ($E > 0.1$ MeV). Loss of the low-energy electrons is not visible on the existing x-ray diagnostic.

For each of the traces B-T in Fig. 6, a SAW pulse of 100 cycles is launched at a starting time between $t = 17$ ms and $t = 40$ ms. As shown in traces B-D in Fig. 6, launched at earlier times the Alfvén wave does not have any impact on the x-ray flux.

Evidence of SAW effectively de-trapping the hot electron population is found in the x-ray flux measurement when the trapped electrons are further accelerated to energies that enable hard x-ray production. Shown in Fig. 6 traces E-J, a burst of x-rays generated by hot electrons escaping the mirror trap and striking metallic surfaces appears during the Alfvén wave propagation time. A large flux of x-ray appears while the Alfvén wave is first turned on. After this initial burst, the x-ray flux decreases as the remaining hot electron population is depleted during the rest of the Alfvén on time. After the Alfvén wave is turned off, the x-ray flux slowly builds up due to the presence of ECRH which remains on until $t = 30$ ms.

After the ECRH terminates at $t = 30$ ms, a population of fast electrons persists in the mirror, and can be de-trapped by launching Alfvén waves at these late times, as evidenced by x-ray bursts in Fig. 6 traces K-T. The estimated trapping time for a 200 keV electron is 40 ms before its loss from cumulative collisions with the helium atoms and ions. The decay of the x-ray burst intensity after $t = 31$ ms reflects the decay of the number of x-ray producing hot electrons still in the mirror. There is also a possible factor of decreasing Alfvén wave amplitude due to the plasma density decay after

the ECRH is switched off, which increases the Alfvén wavelength from 8 m to lengths that no longer fit into the 17 m long plasma column. This measurement proves that the electron loss due to the shear Alfvén wave is not related to the presence of the microwaves.

B. Modulated fast electron loss

The temporal history of the x-ray burst, created by the Alfvén wave de-trapped fast electrons, shows a modulation at the SAW frequency. The x-ray signal, averaged over a large ensemble (1200 shots), is shown in Fig. 7 with comparison of B_x of the shear Alfvén wave measured at the center of the magnetic mirror. The x-ray counting rate can be

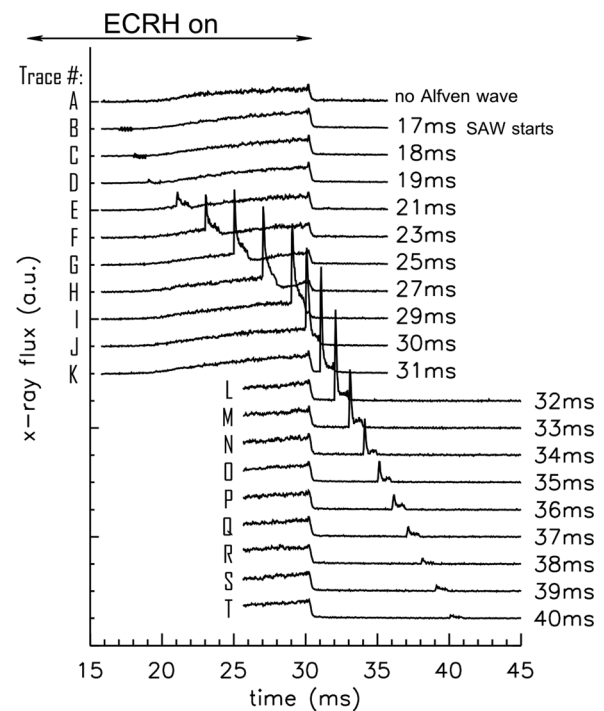


FIG. 6. Time series of x-ray flux measured by an un-collimated detector, designated by letters A-T. The ECRH is on from $t = 0$ to 30 ms, but only after about 20 ms are there sufficient high energy electrons to produce a measurable x-ray flux. Trace A is measured without launching the SAW. In traces B-T a 100 cycle shear Alfvén wave pulse (total duration = 0.87 ms), starting at different times labeled on the graph is launched. Each trace is averaged over 50 plasma shots.

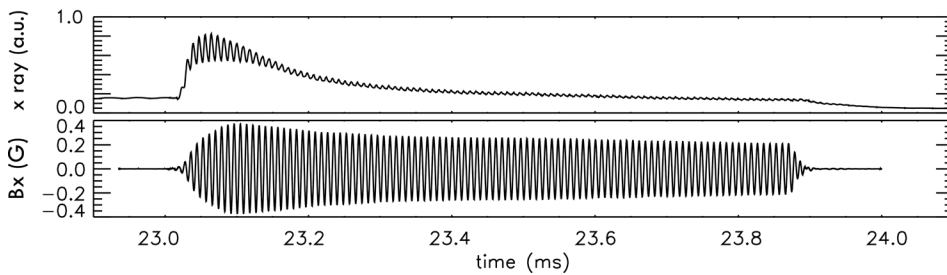


FIG. 7. 1200 shot averaged signal of the x-ray burst during SAW propagation. B_x of the SAW measured at the center of the magnetic mirror in absence of the ECRH is shown on the bottom trace.

reduced by decreasing the detector solid angle. At very low counting rates, the detector receives at most one x-ray over the time of a wave period. Such measurement confirms that the x-rays are created at a fixed phase of the SAW.

C. Spatial distribution of the lost electrons

Because the x-rays are traces of energetic electrons striking a metallic surface, the x-ray emissivity profile can reveal the spatial distribution of the released hot electrons. Hard x-ray computed tomography (CT) is performed, which is a non-invasive diagnostic to measure the spatial profile of x-ray emissivity. Line integrated x-rays are measured on a set of chords using a lead shielded x-ray detector with an acceptance angle defined by a lead pinhole. A data plane usually consists of several hundred chords, one chord per plasma shot. The 2D local emissivity profile is reconstructed by mathematically inverting the chord integrated data. The inverting process adapted a novel Dot by Dot Reconstruction (DDR) method,²⁷ which is found to be more effective than previously published methods for this experiment. Axial tomograms are measured at the center of the mirror and at the LaPD molybdenum mesh anode located at $z = 10.75$ m. Due to imperfect mirror confinement, fast electrons are slowly lost and x-rays are continuously generated at both locations, and are significantly enhanced when a shear Alfvén wave is launched.

The measured tomogram at the center of the magnetic mirror is shown in Fig. 8. The size and position of the waveguide is shown as semi-transparent red rectangles. In this experimental setting, the waveguide is the closest object to the trapped hot electron ring; therefore, the lost hot electrons are

most likely to hit the waveguide. As a result, an intense x-ray emissivity is observed in the region where the waveguide locates.

Fig. 9 shows the tomograms on the transverse plane where the mesh anode was situated. These x-rays are generated when hot electrons escape the mirror along the machine axis, travel along the magnetic field line and strike the anode. The x-ray counting rate measured on the anode is about 2% of that measured near the center of the magnetic mirror. The reconstructed emissivity profile on the anode is shown in Fig. 9. The line cut of the emissivity profile before the Alfvén wave appears to be double peaked at $x = \pm 7$ cm. The magnetic field line at this location can be traced back to $x = \pm 9.2$ cm in the center of the magnetic mirror. The peak on right-hand side of Fig. 9 is located at $x = -6$ cm which corresponds to $x = -7.9$ cm at the mirror center and $x = -5.9$ cm at the RMF antenna.

D. Alfvén ghost

The loss of the fast electrons is observed to continue even after the termination of the Alfvén wave. The hot electron loss is still modulated, at the same frequency that the Alfvén wave when it was on. Shown in Fig. 10(b) is the measured magnetic field of the wave (B_y) at $z = 191.7$ cm. After the driver is shut off, magnetic fluctuations are observed for an additional 4–5 wave cycles, which appear to become incoherent (frequency is decreased and phase is shifted) as shown magnified in Fig. 10(c). About eight SAW periods after the wave driver is turned off, the amplitude of magnetic fluctuation drops to a negligible level (below 0.1 mG).

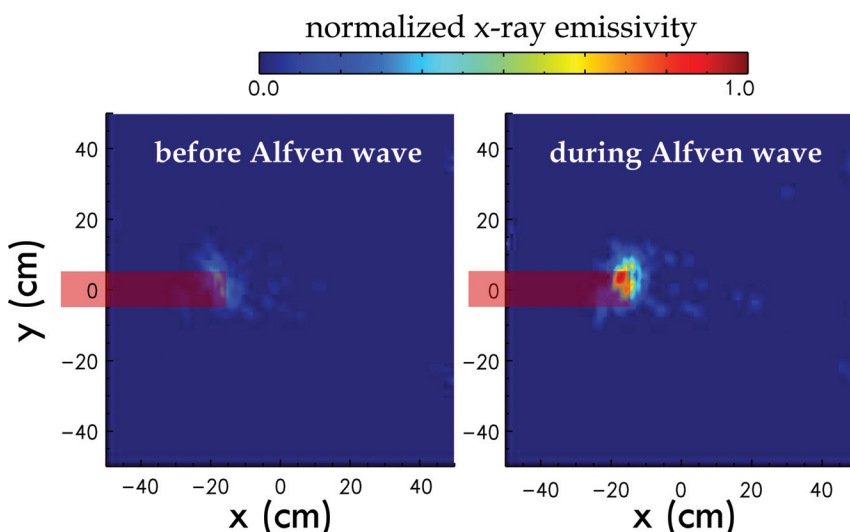


FIG. 8. X-ray axial tomograms at mirror center. The semi-transparent red rectangles indicating the size and position of the waveguide are superimposed in the plots.

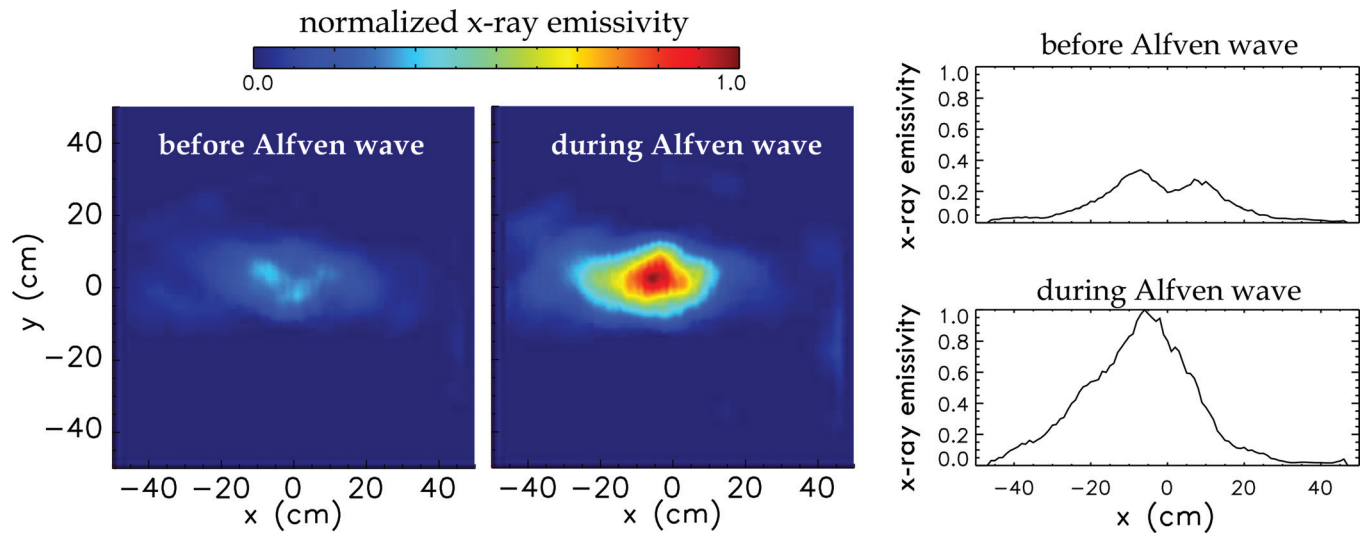


FIG. 9. (Left) X-ray axial tomograms on the plane where the mesh anode was situated ($z = 10.75$ m). (Right) horizontal line cuts at $y = 0$ of the two tomograms.

Even so the hot electrons continue to be lost from the magnetic mirror periodically at the SAW frequency. The x-ray oscillations are observed to last more than 50 cycles coherently after the wave is terminated (Fig. 10(a)). It is likely that the Alfvén wave has left an imprint on the trapped hot electron distribution function that is not damped and de-traps the hot electrons.

E. Deformation of the ring

The temporal oscillation of the x-rays and its continuation after the termination of the Alfvén wave raises the possibility that the injection of the Alfvén wave generates a collective mode of the ring. In this scenario, the collisionless hot electrons interact with each other, likely through a non-local electric field, and oscillate collectively at one frequency. Such a large scale electric field may be directly related to a spatial distortion of the ring, which may come from the non-uniform Alfvén wave field pattern. To study this geometrical asymmetry, a tantalum paddle is inserted to the ring from the side opposite to the waveguide (Fig. 11(a)).

With the asymmetric setups such as cases 1 and 3, as the deformation pattern rotates with the Alfvén wave, electrons

are scraped off by the either waveguide or the tantalum paddle in each Alfvén wave period, thus the x-ray signal (Figs. 11(b) and 11(c)) has a dominant oscillation at $f = f_{\text{Alfvén}}$ ($m = 1$ mode). In these two cases, the phases of the x-ray oscillations are almost reversed. Higher harmonics ($m = 2-4$) also appears in these two cases. In case 2, the ring is shaved by both the waveguide and the paddle. As the ring is forced to be more symmetric, the dominant $m = 1$ oscillation in the x-ray signal is suppressed along with an $m = 3$ mode, while the $m = 2, 4$ oscillation remains. One can imagine that if we make the setup completely cylindrical symmetric, then all modes other than the $m = 0$ will be suppressed, and the de-trapping of the hot electrons will happen at a nearly uniform rate.

F. Dependence of de-trapping on the Alfvén wave polarization

It has been observed that the polarization of the Alfvén wave is important in this experiment. Here, we define the Alfvén wave polarization by the polarization of its magnetic field on the machine axis where the wave amplitude is

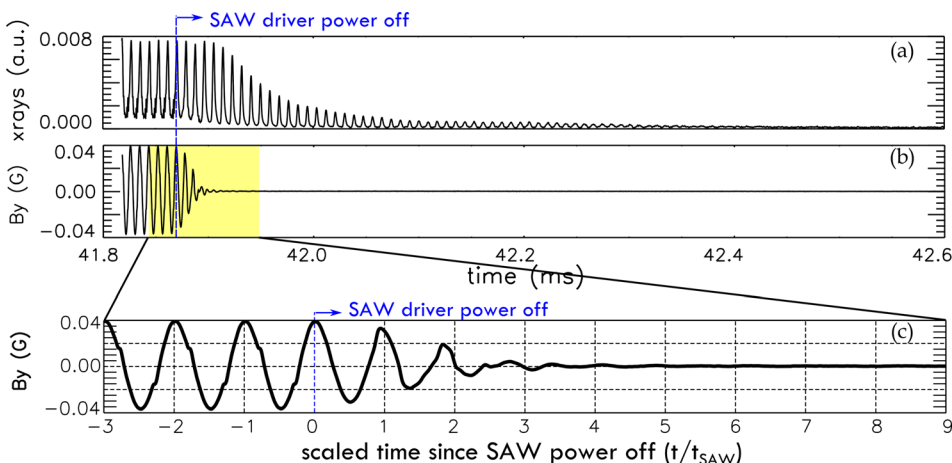


FIG. 10. X-ray flux and B_y of the Alfvén wave on the machine axis outside the mirror, measured just after the Alfvén wave driver power off.

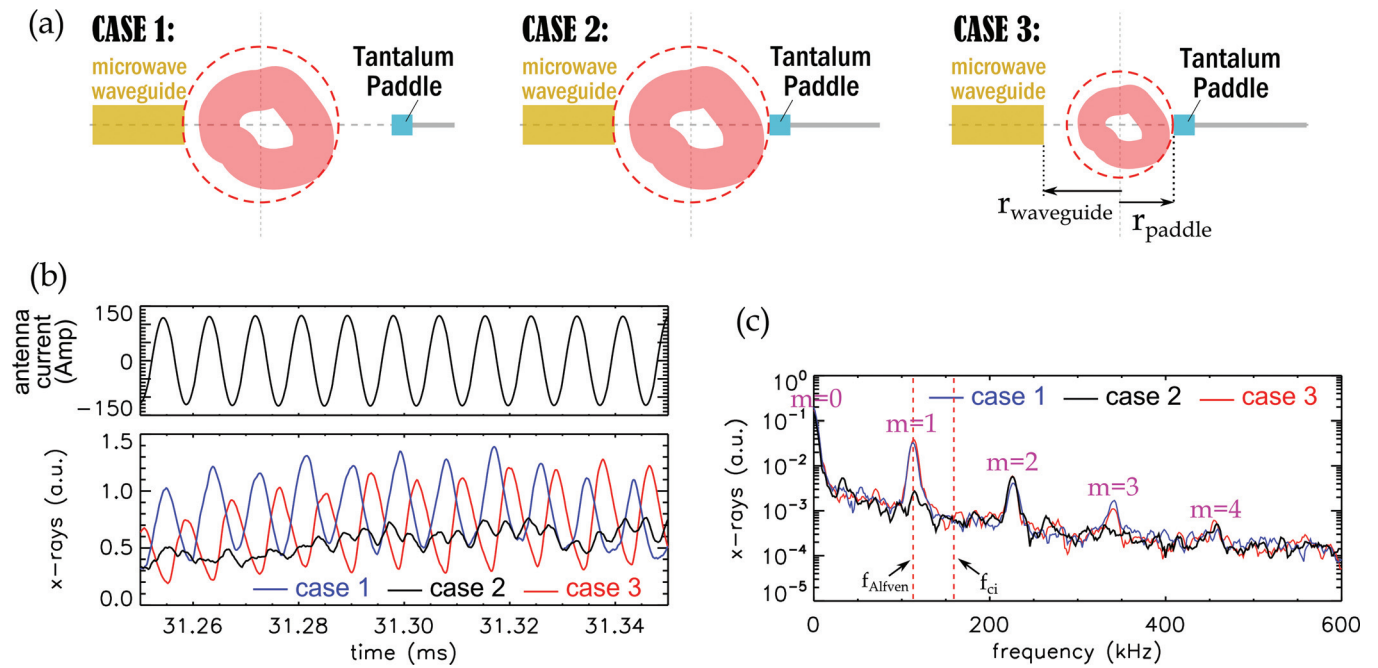


FIG. 11. (a) Cartoon of experiment setup, for three cases with different positions of a tantalum paddle inserted from the opposite side of the waveguide. The hot electrons are shown in pink. (b) X-rays as function of time measured in the three cases. Antenna current is shown on top for comparison. (c) Frequency spectrum of the x-ray signal. The dominant oscillation at $f = f_{\text{Alfvén}}$ is suppressed by compensating geometrical asymmetry of the experiment.

largest, and express it as a combination of left-handed (LH) and right-handed (RH) circularly polarized waves as

$$\begin{pmatrix} \tilde{B}_x \\ \tilde{B}_y \end{pmatrix} = \tilde{B}_{RH} \frac{1}{\sqrt{2}} \begin{pmatrix} 1 \\ i \end{pmatrix} + \tilde{B}_{LH} \frac{1}{\sqrt{2}} \begin{pmatrix} 1 \\ -i \end{pmatrix},$$

where \sim denotes complex amplitudes such that the physical field $B = \text{Re}(\tilde{B}e^{-i\omega t})$. To be clear, here the polarization is

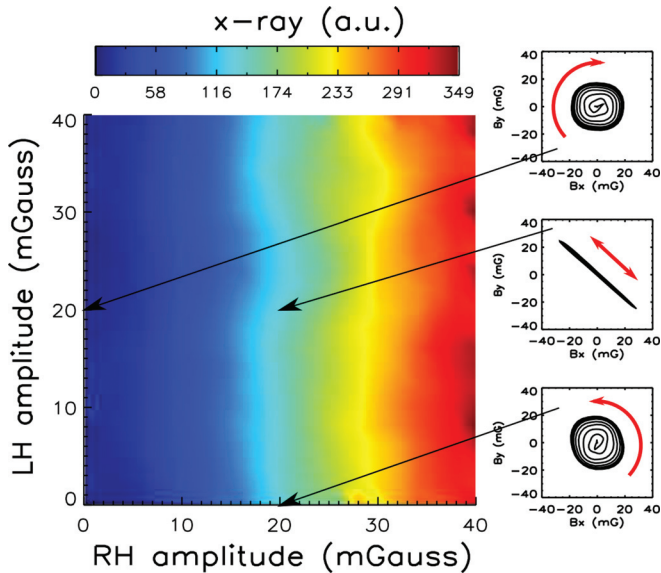


FIG. 12. (Left) The x-ray flux measured when Alfvén waves of different polarizations are launched. (Right col.) Hodograms of Alfvén wave magnetic field with three different polarities. The hodograms begin at the center ($B_x = 0$, $B_y = 0$) when the wave is first turned on at $t = 31$ ms and last for 11 SAW cycles, with red arrows indicating the directions the $B_{\text{Alfvén}}$ vectors evolve as time advances. The wave magnetic field is measured by a 3-axis B-dot probe on the machine axis at $z = 191.7$ cm, by which the polarity of the wave is determined.

defined with respect to the background magnetic field, and the RH direction is the electron gyro-motion direction.

The Alfvén waves are launched with 441 different polarizations to study their effect on the trapped hot electrons. The transverse magnetic field of the wave is measured at $z = 191.7$ cm on the magnetic axis, and the polarization of each wave determined and characterized by the amplitudes of the two circularly polarized components ($|\tilde{B}_{RH}|$, $|\tilde{B}_{LH}|$). Hodograms of the measured B field of three different waves are shown in Fig. 12 as examples. The hot electron ring is created by ECRH from $t = 0$ to $t = 30$ ms, and the waves are launched at $t = 31$ ms for 20 cycles. The color map in Fig. 12 is the total x-ray flux generated by Alfvén wave de-trapped hot electrons. The nearly vertical contours indicate the de-trapping is only related to the RH component, while the LH component does not affect the de-trapping.

The x-ray oscillation at the Alfvén wave frequency, such as one shown in Fig. 7, can be approximated by a sine function, thus we can define the phase of the x-ray oscillation. In order to study the relationship between the phase of the x-ray oscillation and that of \tilde{B}_{RH} and \tilde{B}_{LH} , another 441 shear Alfvén waves are launched, each with a distinct polarization composed of RH and LH of the same amplitude but with different phases. Such waves are all linearly polarized but with different polarization directions (3 examples are shown in Fig. 13). The phase of the x-ray oscillation as a function of the phases of RH and LH is shown in Fig. 13. The vertical contour indicates the x-ray oscillation is also phase locked to the RH component, and not related to the LH component.

G. X-ray spectrum

The spectrum of the hard x-rays is obtained by pulse-height-analysis from the scintillator detector response, and is

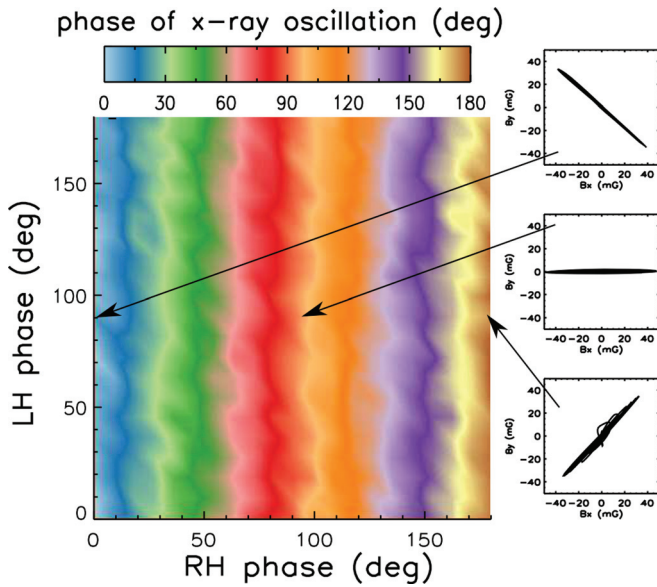


FIG. 13. (Left) phase of x-ray modulation at $f_{\text{Alfvén}}$ as a function of phases of LH and RH component of the Alfvén wave. For ease of comparison, the relative phases are shown with the smallest phases set to 0° (Right col.) Hodograms of three Alfvén waves transverse magnetic field measured by a B-dot probe on machine axis at $z = 191.7$ cm.

calibrated with the 661.7 keV x-ray emission of Cesium-137. Fig. 14(a) shows the spectrum of x-rays generated at the center of the magnetic mirror. Without the presence of Alfvén waves, the hot electrons are slowly lost due to collisions and magnetic field errors. The spectrum overall shows an exponential decay with an e-folding energy of $\Delta E = 37.4$ keV. The deviation from the exponential decay below 100 keV is caused by the low x-ray transmission coefficient of the stainless steel wall of the vacuum vessel. The x-ray counting rate, over the entire energy spectrum, is significantly increased

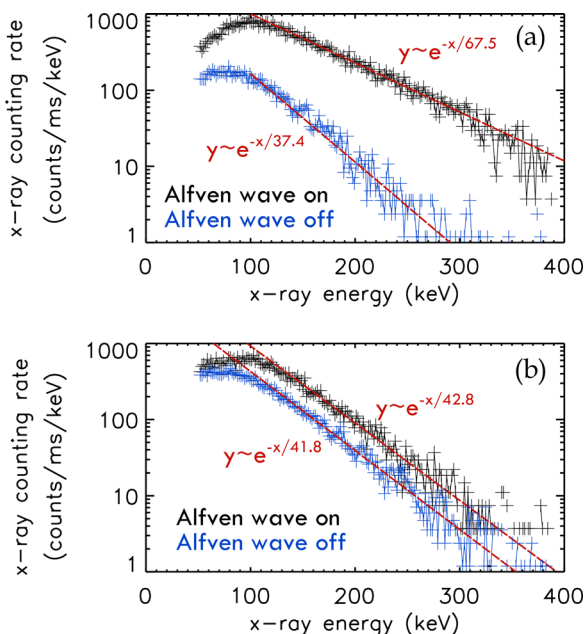


FIG. 14. X-ray spectrum measured with/without the presence of shear Alfvén wave (a) near the center of the magnetic mirror; (b) at one end of the magnetic mirror.

when the Alfvén wave is launched. The x-ray spectrum when the Alfvén is launched still appears to be exponentially decaying with an e-folding energy $\Delta E = 67.5$ keV.

The spectrum of the x-rays generated by the axially lost electrons (striking a wire mesh inserted at $z = 351.5$ cm) is plotted in Fig. 14(b). Similar exponential decay is shown above 100 keV, with $\Delta E = 41.8$ keV (no Alfvén wave) and $\Delta E = 42.8$ keV (with Alfvén wave), respectively. The counting rate is doubled by the Alfvén wave almost uniformly over the whole energy spectrum.

H. Whistler waves and electron de-trapping

The de-trapping process is found to be accompanied by electro-static fluctuations in the frequency range of $1 \sim 5f_{ih}$ (the lower hybrid frequency $f_{ih} = (f_{ci}f_{ce})^{1/2}$ is about 30 MHz in this case), which are also modulated at the Alfvén wave frequency (Fig. 15(a)). The electric fluctuations are measured by an electric dipole probe located outside the mirror at $z = 1.91$ m. They are most likely caused by the high harmonics in the rf current driven in the RMF antenna.

To exclude the possible role of these high frequency fluctuations in the electron de-trapping process, whistler waves at these frequencies are launched with a loop antenna in absence of the Alfvén wave. The electric field amplitudes of the launched whistler waves are at least 10 times higher than that of the high frequency fluctuations accompanied by the electron de-trapping. No significant electron de-trapping is observed when the whistler waves are launched (Fig. 15(b)).

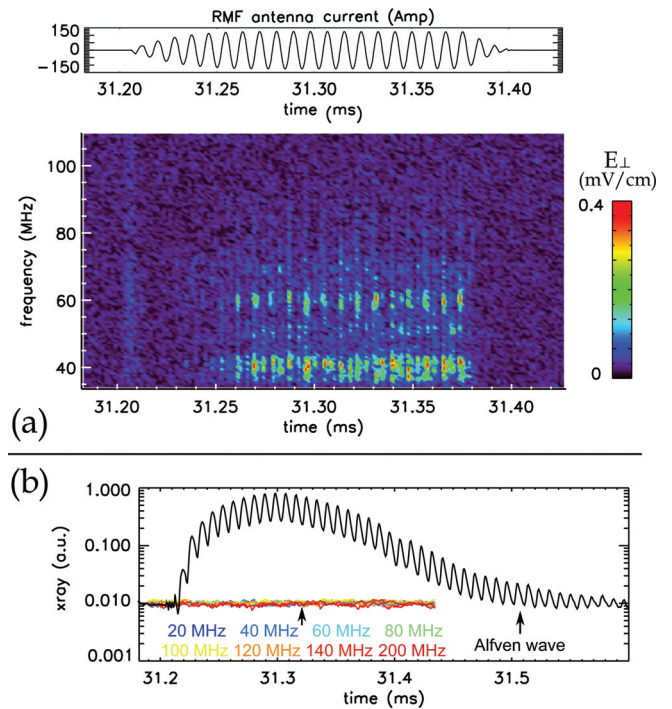


FIG. 15. (a) High frequency electro-static fluctuations are found to accompany the electron de-trapping process. Current in the RMF antenna is plotted on top for comparison. The launched Alfvén wave has 20 cycles at 115 kHz. (b) X-ray signal measured when Alfvén wave (115 kHz) or whistler waves (20–200 MHz) are launched. In both cases, a hot electron ring is generated by ECRH on from $t = [0, 30]$ ms. The Alfvén wave is on from $t = [31.2, 31.37]$ ms. The whistler waves are turned on from $t = [31.2, 31.3]$ ms.

IV. DISCUSSION AND CONCLUSIONS

The hard x-ray tomography shows electrons are lost in both the radial and axial direction of the magnetic mirror. Of special interest are the axially lost electrons, as such electron losses have direct implication for radiation belt remediation, which is the primary motivation of this study. The electrons are well confined by the mirror field in absence of the Alfvén wave, with a measured lower limit of pitch-angle distribution well above the loss cone (9° gap, i.e., for a 100 keV electron $\Delta E_{\parallel} \geq 15$ keV is required to reach the loss cone). Analysis of the electron single particle motion shows that in order to break its first adiabatic invariant $\mu = \frac{p_{\perp}^2}{2mB}$ and change its pitch angle to reach the loss cone, at least a 10% perturbation of the background field is required. This is very unlikely to be the case in the experiment, where the wave field is measured to be 0.1% of B_0 .

The periodic loss of the electrons is found to be caused only by the RH circularly polarized component of the Alfvén wave. When a LH wave is applied, no x-rays are produced; when a LH wave is mixed with a RH wave, the effect on the x-rays is the same as that caused by only the RH wave component. This means that the LH polarized wave passes through the hot electron ring and does not interact with it at all. At the time scale of electron gyro-period, the SAW is essentially stationary, thus the different polarizations are not distinguished by means of electron gyration. Another type of electron motion in the perpendicular direction is the azimuthal drift, which is also in the RH direction. The calculated frequency of this drift motion ranges from 50 kHz to 600 kHz for the electron energies and pitch angles measured in the experiment, which is comparable to the frequency of the SAW. Therefore, it is possible that the different polarizations are distinguished by mechanisms associated with the azimuthal rotation of the electron ring.

The experimental observations of the continued electron loss after the termination of the SAW and the spatial distortion of the ring strongly suggest that a collective mode of the ring is created by a RH polarized SAW. As shown in Fig. 5, the SAW field is highly non-uniform over the hot electron ring region ($5 \text{ cm} < r < 15 \text{ cm}$). It is conjectured that such non-uniform wave field pattern distorts the spatial shape of the ring via the hot electron $\vec{E}_{\text{Alfvén}} \times \vec{B}_0$ drift. If the electron guiding center azimuthal drift motion is in phase with the rotation of the SAW pattern, then the drift does not change direction for a long period of time, therefore the displacement of the guiding center accumulates and the ring deformation grows. This scenario is similar to the drift-resonance²⁸ often studied in space physics. The electric field of the Alfvén wave is estimated to be $E_{\perp} = 0.5 \text{ V/cm}$. At this amplitude, the time it takes to displace the electron guiding center by 1 cm is about one Alfvén wave cycle. Such drift resonance, between a fraction of the ring electrons and the shear Alfvén wave, can amplify the three dimensional spatial distortion of the ring and may establish a large scale global electric field, through which the collisionless hot electrons interact with each other to create a collective mode of the ring that affects its confinement and leads to electron loss in the axial or radial direction. This collective mode may

de-trap electrons over a wide range of energies, even for those not in drift-resonance with the Alfvén wave (as shown in Fig. 14), and can persist after the drift-resonance disappears (as shown in Fig. 10).

This study can be further explored with a detailed theoretical model of the collective behavior of a distorted hot electron ring, which is very likely also coupled to the cold background plasma, to eventually understand the mechanism causing the axial loss of the electrons from the magnetic mirror. Such model may even potentially lead to innovative schemes to artificially modify the profile of the ring current drifting in the Earth's magnetic field, to catalyze the change in dynamics of radiation belts and the subsequent remediation.

ACKNOWLEDGMENTS

This work was supported by the Office of Naval Research under ONR MURI award 00014-07-1-0789 and performed at the Basic Plasma Science Facility at UCLA, which is funded by the Department of Energy and the National Science Foundation. The authors would like to thank Z. Lucky, M. Drandell, and M. Nakamoto for their valuable technical help and Professor G. Morales for insightful comments. The authors also thank the referee for helpful suggestions on revising the paper.

- ¹W. Gekelman, H. Pfister, Z. Lucky, J. Bamber, D. Leneman, and J. Maggs, *Rev. Sci. Instrum.* **62**(12), 2875–2883 (1991).
- ²Satellite Industry Association, 2012 SIA State of the Satellite Industry Report (2012).
- ³U. S. Inan, T. F. Bell, J. Bortnik, and J. M. Albert, *J. Geophys. Res.* **108**(A5), 1186, doi:10.1029/2002JA009580 (2003).
- ⁴R. B. Horne, S. A. Glauert, and R. M. Thorne, *Geophys. Res. Lett.* **30**(9), 1493, doi:10.1029/2003GL016963 (2003).
- ⁵J. Bortnik, R. M. Thorne, T. P. O'Brien, J. C. Green, R. J. Strangeway, Y. Y. Shprits, and D. N. Baker, *J. Geophys. Res.* **111**(A12), A12216, doi:10.1029/2006JA011802 (2006).
- ⁶D. L. Turner, Y. Shprits, M. Hartinger, and V. Angelopoulos, *Nat. Phys.* **8**(3), 208–212 (2012).
- ⁷R. M. Thorne and C. F. Kennel, *J. Geophys. Res.* **76**(19), 4446–4453, doi:10.1029/JA076i019p04446 (1971).
- ⁸R. M. Millan and R. M. Thorne, *J. Atmos. Sol.-Terr. Phys.* **69**(3), 362–377 (2007).
- ⁹H. I. West, R. M. Buck, and J. R. Walton, *Nature* **240**(97), 6–7 (1972).
- ¹⁰S. Ohtani, Y. Miyoshi, H. J. Singer, and J. M. Weygand, *J. Geophys. Res.* **114**(A1), A01202, doi:10.1029/2008JA013391 (2009).
- ¹¹D. H. Brautigam and J. M. Albert, *J. Geophys. Res.* **105**(A1), 291–309, doi:10.1029/1999JA900344 (2000).
- ¹²Y. Y. Shprits, R. M. Thorne, R. Friedel, G. D. Reeves, J. Fennell, D. N. Baker, and S. G. Kanekal, *J. Geophys. Res.* **111**(A11), A11214, doi:10.1029/2006JA011657 (2006).
- ¹³Y. Wang, W. Gekelman, P. Pribyl, and K. Papadopoulos, *Phys. Rev. Lett.* **108**, 105002 (2012).
- ¹⁴T. M. Loto'aniu, H. J. Singer, C. L. Waters, V. Angelopoulos, I. R. Mann, S. R. Elkington, and J. W. Bonnell, *J. Geophys. Res.* **115**(A12), A12245, doi:10.1029/2010JA015755 (2010).
- ¹⁵T. Brito, L. Woodger, M. Hudson, and R. Millan, *Geophys. Res. Lett.* **39**(22), L22104, doi:10.1029/2012GL053790 (2012).
- ¹⁶A. W. Degeling, R. Rankin, K. Murphy, and J. Rae, *J. Geophys. Res.* **118**(6), 2919–2927, doi:10.1002/jgra.50219 (2013).
- ¹⁷S. R. Elkington, M. K. Hudson, and A. A. Chan, *Geophys. Res. Lett.* **26**(21), 3273–3276, doi:10.1029/1999GL003659 (1999).
- ¹⁸T. P. O'Brien, K. R. Lorentzen, I. R. Mann, N. P. Meredith, J. B. Blake, J. F. Fennell, M. D. Looper, D. K. Milling, and R. R. Anderson, *J. Geophys. Res.* **108**(A8), 1329, doi:10.1029/2002JA009784 (2003).

- ¹⁹N. Sato, K. Hayashi, S. Kokubun, T. Oguti, and H. Fukunishi, *J. Atmos. Terr. Phys.* **36**(9), 1515–1526 (1974).
- ²⁰H. Ikegami, H. Ikezi, M. Hosokawa, S. Tanaka, and K. Takayama, *Phys. Rev. Lett.* **19**(14), 778 (1967).
- ²¹W. Gekelman, S. Vincena, D. Leneman, and J. Maggs, *J. Geophys. Res.* **102**, 7225–7236, doi:10.1029/96JA03683 (1997).
- ²²W. Gekelman, D. Leneman, J. Maggs, and S. Vincena, *Phys. Plasmas* **1**(12), 3775–3783 (1994).
- ²³A. Gigliotti, W. Gekelman, P. Pribyl, S. Vincena, A. Karavaev, X. Shao, A. S. Sharma, and D. Papadopoulos, *Phys. Plasmas* **16**(9), 092106 (2009).
- ²⁴A. V. Karavaev, N. A. Gumerov, K. Papadopoulos, X. Shao, A. S. Sharma, W. Gekelman, Y. Wang, B. Van Compernelle, P. Pribyl, and S. Vincena, *Phys. Plasmas* **18**(3), 032113 (2011).
- ²⁵G. J. Morales, R. S. Loritsch, and J. E. Maggs, *Phys. Plasmas* **1**(12), 3765–3774 (1994).
- ²⁶N. Palmer, W. Gekelman, and S. Vincena, *Phys. Plasmas* **12**(7), 072102–072102–12 (2005).
- ²⁷Y. Wang, W. Gekelman, and P. Pribyl, *Rev. Sci. Instrum.* **84**(5), 053503 (2013).
- ²⁸J. G. Roederer, *Dynamics of Geomagnetically Trapped Radiation* (Springer, New York, 1970).